

## NOVEL NOLEN MATRIX BASED BEAMFORMING NETWORKS FOR SERIES-FED LOW SLL MULTIBEAM ANTENNAS

Fanourios E. Fakoukakis and George A. Kyriacou\*

Microwaves Laboratory, Dept. of Electrical & Computer Engineering, Democritus University of Thrace, Xanthi GR-67100, Greece

**Abstract**—A new type of cascaded series feed beamforming networks (BFNs) is introduced. The network architecture is based on a dual-series Nolen matrix topology. It is able to produce tapered output amplitude distributions from  $N \times N$  configurations. The general concept, analysis and systematic design of the BFNs are given. The networks are designed and intended to be used mainly for low Sidelobe Level (SLL) linear Multibeam Antennas (MBAs). Several design examples are presented, along with fabrication and measurements of an S-band prototype.

### 1. INTRODUCTION

Multibeam antennas have been in the forefront for several decades. Their development mainly arose through the research in beamforming matrices. Mainly, an MBA is composed of a linear antenna array fed by a multiple input-multiple output beamforming network (matrix or lens). BFN provides an array with appropriate amplitude and phase excitations, whereas each BFN input port corresponds to a discrete radiated beam in space. Thus, on transmit mode, multiple independent beams can be created from a single aperture through the sequential excitation of BFN input ports. On the other hand, all beams are simultaneously available on receive mode. Multibeam antennas are extensively used in satellite communications, but also in radar and electronic warfare systems and point-to-multipoint ground communications [1–3].

In general, multiple beam feeds are divided into two main categories, according to the feeding method; that is, parallel

---

*Received 16 January 2013, Accepted 4 March 2013, Scheduled 17 April 2013*

\* Corresponding author: George A. Kyriacou (gkyriac@ee.duth.gr).

(corporate) and series feeds [1–3]. The most widely known beamforming matrices are the Butler [1–6], Blass [7] and Nolen [8] matrices. The Butler matrix is a corporate multiple beam feed, whereas Blass and Nolen matrices exploit the series feed method. While Butler matrix is usually designed with an equal number of input (beam) and output (antenna) ports ( $N \times N$ ), Blass and Nolen matrices can be readily designed with an unequal number of inputs and outputs ( $M \times N$ ). However, some early and recent works have reported Butler matrices with unequal numbers of inputs and outputs, implementing low SLL distributions [4, 9–11].

Whereas the Butler matrix has received a great interest, having been under a vast amount of research efforts and been used in a variety of applications, Blass and Nolen matrices have not received much attention. That is mainly due to the comparative advantages Butler matrix appears with respect to the other two counterparts. However, some research efforts on Blass and Nolen matrices have been published recently [12–15], which make use of a computer coded algorithm for the design of the networks. This algorithm is initially introduced in [12] and aims mainly at the determination of the optimum network device values in order to minimize power dissipation and maximize efficiency in Blass matrix networks, which suffer from power losses on the terminated loads. Especially in [13], an improved algorithm is used, compared to [12], which allows for the creation of beams pointing in arbitrary positions and can be also implemented for non-orthogonal output amplitude and phase excitations. Lastly, in [14, 15] a singular case of the algorithm is used since no terminated loads are needed in Nolen matrix networks. The approach followed in this work was found to be more convenient but mostly, more extendable to Nolen matrices (and Nolen matrix based networks) of arbitrary number of antennas (output ports) and radiated beams (input ports).

We have also published some work on Butler matrix and Butler matrix-based BFNs [16–18]. However, in this work, the research effort is focused on a novel type of series feed  $N \times N$  BFN based on a dual-series Nolen matrix architecture. The design of optimally efficient dual-series networks was presented in [19], however the procedure used therein cannot be extended to higher numbers of input ports.

In general, although series feed BFNs present some disadvantages over the corporate networks, such as the larger number of elements used (couplers, phase shifters), they also own critical assets, such as the avoidance of transmission line crossings. Moreover, not any arbitrary tapered output amplitude distribution can be implemented with Butler-like corporate BFNs, due to constraints imposed by the conservation of energy principle, the limitations on the coupling

ratio of the asymmetric couplers and the restrictions in the parallel circuit connections of the network configuration. On the other hand, series networks are theoretically able to form any arbitrary amplitude distribution. Lastly, while corporate networks are mainly used in phased arrays systems, series networks can also be distinctively used in frequency scanning arrays. Among the Blass and Nolen matrix, the latter seems more attractive, offering higher circuit efficiency and less amount of complexity, while using fewer elements. In fact, the Nolen matrix architecture emerges from a simplification of the Blass matrix.

To the authors' knowledge, a Nolen matrix with low SLL distribution and equal number of inputs and outputs has not been reported. Only a  $4 \times 8$  low SLL Nolen matrix has been published recently [15]. In fact, it is impossible to design an  $N \times N$  Nolen matrix with a tapered amplitude distribution, due to contradictions in the energy conservation principle. That is, as it is proven and referred in [20–22], low SLL radiation patterns (as a result of tapered amplitude distributions) can only be achieved by lossy  $N \times N$  networks. Thus, lossy  $N \times N$  networks can produce low SLL MBAs, where beam orthogonality is cancelled due to an increase in Half-Power Beam-Width (HPBW), which also leads to an increase in beam Crossover Level (CL). Moreover, the losses can be minimized according to Stein's limit [23]. The Nolen matrix, as a theoretically lossless network, can only produce uniform amplitude distributions, creating orthogonal beams with a SLL of about  $-13.2$  dB. Making the number of outputs ( $N$ ) larger than the number of inputs ( $M$ ) enables for the creation of tapered amplitude distributions and also offers a reduction in HPBW of the radiation pattern beams, leading to more accurate beam-pointing, [9–11, 15]. Therefore, increasing the number of antenna elements, and thus the electrical size of the array, leads to an opposing reduction in HPBW that could restore orthogonality (although CL is correspondingly decreased). However, scanning efficiency is deteriorated due to the large angular distance of beam maxima, which can be far greater than a beamwidth.

Taking all the above into account, a novel Nolen matrix based modified topology was utilized in order to design the architecture of the BFNs presented herein. Apart from the use of a dual-series subnetwork as the basic building block, the design idea is based on the insertion of losses in the network. Thus, according to the above, the lossy network can now be designed to produce low SLL non-orthogonal beams. The case of unequal numbers of inputs and outputs is also described. The emphasis is again given on the design of networks offering low SLL characteristics to the matrix fed multibeam antenna.

## 2. NETWORK SYNTHESIS RATIONALE

### 2.1. Nolen Matrix Review

The schematic diagram of an  $N \times N$  Nolen matrix is presented in Figure 1(a). It is consisted of four-port directional couplers ( $\theta$ -devices) and phase shifters ( $\Phi$ -devices). The value of  $\theta$  determines the coupler's amplitude coupling coefficient, as shown in Figure 1(b). The Nolen matrix is a generalization of the Butler matrix [1, 8], in which it can be reduced. Basically, the Nolen matrix topology is the analog circuit implementation of the general Discrete Fourier Transform (DFT) algorithm, which can be applied to any number of elements, even prime numbers. Therefore, it can be reduced to simpler forms, as the Fast Fourier Transform analog equivalent Butler matrix, which can be applied only to arrays with element number  $N = 2^n$  [1]. In Figure 1(a), the number of input ports is equal to the number of output ports; however, it can be also designed having the number of inputs unequal to the number of outputs.

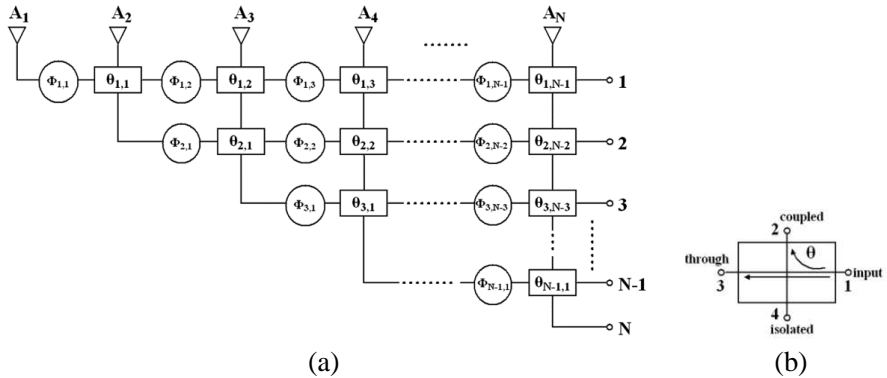


**Figure 1.** (a) Nolen matrix schematic diagram. (b) Directional coupler ( $\theta$ -device) basic function.

The voltage transfer function characteristics ( $S$ -parameters) of the directional couplers are schematically presented in Figure 2.

In order for the network to be able to produce a certain predetermined radiation pattern, the array excitation coefficients must be calculated. Thus, aiming at a specific radiation pattern, classic array synthesis techniques can be utilized to evaluate the necessary amplitude and phase of the excitation coefficients at the antenna element inputs ( $a_{n,i}$ ,  $n$  = matrix input port,  $i$  = antenna port), e.g., [2]. In turn, for a steerable phased array the excitation phase sequences can

be obtained. Then, once the array distribution is specified, the values of  $\theta$  and  $\Phi$  for the whole Nolen matrix can be finally determined, following a cascaded series microwave network design approach.

Explicitly, starting from Figure 3 an iterative procedure is followed based on a recursive set of equations describing the behavior of a small part of the network. Taking into account the transfer function characteristics of the directional couplers (Figure 2), the excitation coefficients ( $\alpha_{n,1}, \alpha_{n,2}$ ) of antenna elements  $A_1$  and  $A_2$  when input port  $n$  is excited at the first step of the iterative procedure are given by the derived equations for the leftmost subnetwork of Figure 3, which read:

$$a_{n,1} = a'_{n,1} \cos \theta e^{j(\phi-\pi)} + a''_{n,2} \sin \theta e^{j\phi} \tag{1a}$$

$$a_{n,2} = a'_{n,1} \sin \theta e^{j\theta} + a''_{n,2} \cos \theta e^{j\theta} \tag{1b}$$

While the power conservation principle requires that:

$$(a'_{n,1})^2 + (a''_{n,2})^2 = (a_{n,1})^2 + (a_{n,2})^2 \tag{1c}$$

Thus, in order to determine the values of the first  $\theta$  and  $\Phi$  device shown in Figure 3 (denoted as  $\theta_{1,1}$  and  $\Phi_{1,1}$  in Figure 1(a)), (1) is solved for  $n = 1$ , implying port  $n = 1$  excitation. The values of the rest of the  $\theta$  and  $\Phi$  devices in the first row are subsequently calculated by applying consecutive further circuit reductions and recursively applying (1).

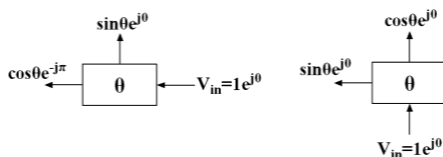


**Figure 2.** Voltage transfer function characteristics of the directional couplers.

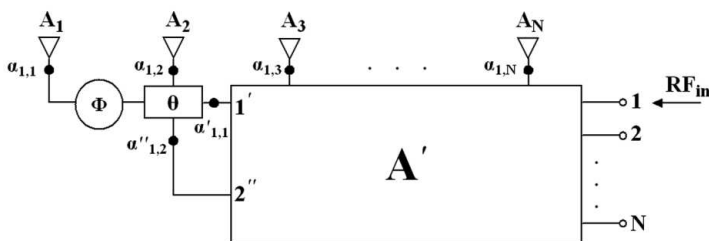


**Figure 3.** Reduced schematic diagram of the Nolen matrix at the first step of the iterative procedure.

## 2.2. General Network Synthesis for Arbitrary Amplitude Distributions

The synthesis of the networks is based on the use of a dual-series Nolen matrix type architecture. The schematic diagram of the basic dual-series network is presented in Figure 4, where it is shown that the isolated unused ports of the second row couplers are terminated.

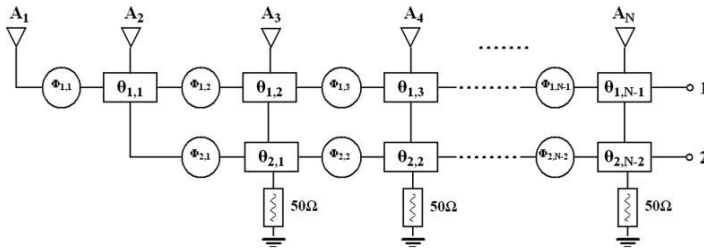


**Figure 4.** Schematic diagram of the basic dual-series ( $2 \times N$ ) network.

As mentioned above, the design of an  $N \times N$  Nolen matrix with a tapered output amplitude distribution (aiming at SLL reduction) presents critical difficulties, since the network is theoretically lossless. A tapered amplitude distribution can be achieved only when the number of output (antenna) ports is larger than the number of input (beam) ports ( $N > M$ ) [15]. However, when the number of inputs is equal to the number of outputs, the design is valid only for a dual-series network. Therefore, the original  $N \times N$  Nolen matrix architecture is reduced to a  $2 \times N$  network, which can be designed for any arbitrary output amplitude and phase distribution for both port 1 and port 2 excitation cases.

The synthesis of networks comprising larger input port numbers ( $M = 2^k$ ) is utilized by gradually combining smaller scale  $M \times N$  networks, where  $M_{k+1} = 2M_k$ . The two subnetwork antenna ports ( $A_1-A_N$ ) are connected in pairs through 3 dB power combiners, as shown in Figure 5(a), where an example of a  $4 \times N$  network is presented, designed by combining two separate  $2 \times N$  subnetworks. The power combiner is used in order to feed the antenna elements with signals coming from the two separate  $2 \times N$  subnetworks. The feeding signals are coming from one  $2 \times N$  subnetwork at a time, regarding the input (beam) port that is activated. These subnetworks are in turn combined, as shown in Figure 5(a), to implement a  $4 \times N$  network or higher order networks. A distinctive point in this procedure is the fact that, since all the  $2 \times N$  subnetworks are designed to create the same output amplitude distribution, the corresponding  $\theta$ -values of all the

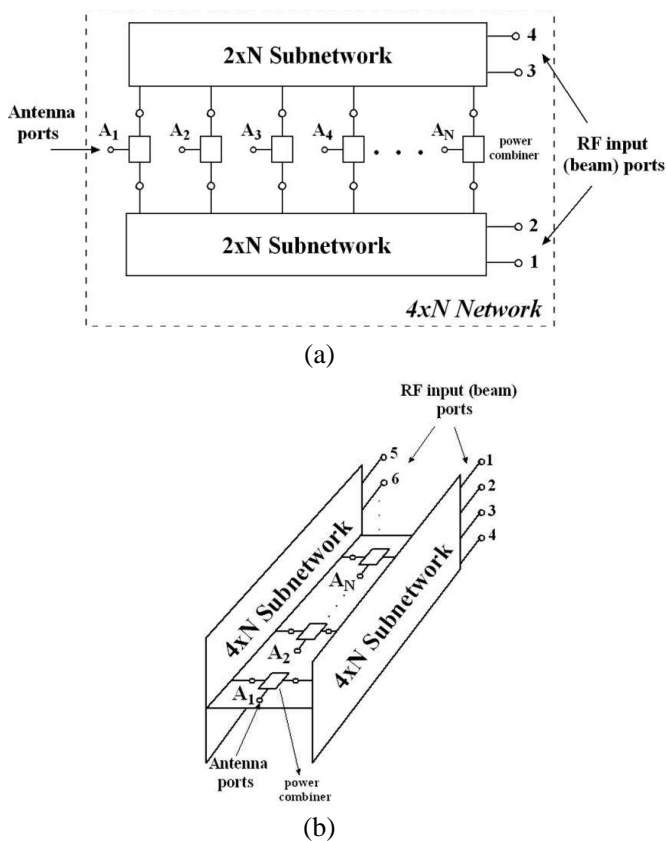


**Figure 5.** (a) Schematic diagram of a planar  $4 \times N$  network composed of two separate  $2 \times N$  subnetworks. (b) Schematic diagram of an  $8 \times N$  brick-type configuration network using two separate planar  $4 \times N$  subnetworks.

subnetworks comprising a higher order network are the same. Thus, once the  $\theta$ -values of one of the  $2 \times N$  subnetworks are determined, no further calculations are needed for the rest subnetworks. On the other hand, since each input (beam) port excitation must create a different output phase distribution (phase progression between antenna elements), creating a different radiated beam in space, once the  $\Phi$ -values of one of the  $2 \times N$  subnetworks are calculated, the values of the rest of the subnetworks can be determined either by just inverting the corresponding values or by simple extrapolation. If still that is not feasible, the procedure is repeatedly applied using recursive equations such as (1), keeping in mind that the  $\theta$ -values are now already known.

For a further increase in the number of input ports (and radiated beams), two separate  $4 \times N$  subnetworks can be combined once again at the antenna terminals through 3 dB power combiners, creating an  $8 \times N$  network in a brick-type configuration, as shown in Figure 5(b). The procedure can be applied successively in the same manner for even larger numbers of input ports ( $16 \times N$ ,  $32 \times N$ , etc.). However, the planar single layer form of the circuit can be retained only up to  $4 \times N$  networks. For larger numbers of input ports, multilayer or brick-type topologies have to be realized, in order to avoid the presence of large numbers of transmission line crossings. It is expected that the well established by now, multilayer LTCC (Low Temperature Co-fired Ceramic) technology is best suited for this brick-type circuits. Moreover, the synthesis of higher order networks demands for more rows of cascaded power combiners at the antenna port level. For example, in the  $8 \times N$  network, each  $4 \times N$  subnetwork uses a row of 3 dB power combiners (Figure 5(a)), each one of them being connected to a corresponding 3 dB power combiner on the central panel (Figure 5(b)). Thus, each antenna port is connected to the network through a 4 input-1 output power combiner. The basic drawback of this configuration is that the losses are increased by a 3 dB amount (assuming that Wilkinson power combiners are adopted) with each added row of combiners (total of 6 dB for the  $8 \times N$  network case).

In order to achieve higher network efficiency, increased beam-pointing accuracy and fully exploit angular sector coverage, the final number of input ports ( $M$ ) should be equal to the number of output ports (antenna elements,  $N$ ). In that way, the capabilities of the network are fully exploited.

It must be noted that the networks are unavoidably made lossy through the use of the power combiners connected at the output-antenna ports. Wilkinson combiners or 3 dB hybrid couplers can be used. In the case of the Wilkinson combiners, the losses arise from the asymmetry due to the activation of one input port at a time, resulting to a voltage difference between the two input ports. This voltage difference creates a leakage current on the resistor branch between the two ports, which is dissipated on the ohmic resistor connected between them. This dissipative loss accounts for the half of the input power ( $-3$  dB). On the other hand, when 4-port 3 dB hybrid couplers are used, one of the two output ports must be terminated, while the other is connected to the antenna. As a result, one half of the input power is again lost on the terminated load. Thus, the 3 dB losses expected constitute the optimum (minimum) theoretical value. Furthermore, as mentioned above, these losses are increased by a 3 dB amount each time the number of input (beam) ports is increased (doubled,  $M_{k+1} = 2M_k$ ),

since another row of 3 dB combiners is added on each step of the procedure.

At this point it must be emphasized that the design procedure adopted herein follows a simpler and more convenient approach compared to the previous efforts ([12–15]), which make use of a specialized algorithm in order to calculate the  $\theta$  and  $\Phi$ -values, as was referred in the introduction. On the contrary to what is employed by Casini et al. in [13], which uses an improved algorithm, this work exploits a simple linear equation system shown in (1) and recursively applies it to a dual-series network to determine the demanded network device values. It is important to notice that no effort for improving efficiency is demanded, since the basic  $2 \times N$  dual-series network configuration requires no power dissipating terminated loads itself. The only amount of power being lost is the part that is unavoidably dissipated on the power combiners connected at the antenna ports, however, these combiners do not contribute to the formation of the output amplitude/power distribution. Moreover, the present design procedure offers comparative advantages, such as the straight-forward, time and resources-saving design for any number of antennas or input (beam) ports and for any arbitrary output amplitude distribution.

Lastly, it must be made clear that the circuit synthesis and design procedure presented in this section could be readily applied for the design of networks with uniform amplitude distributions. Although a conventional Nolen matrix could be designed instead, the dual-series nature of the networks presented herein makes the determination of  $\theta$  and  $\Phi$ -values much easier.

### 3. DESIGN EXAMPLES

In order to verify the design concept, several design architectures were investigated. Complete networks were designed and simulated. All networks are able to create tapered output distributions, producing low SLL antenna array radiation patterns. The circuits were designed in microstrip form. The  $\Phi$ -devices phase shifters were realized using meandered microstrip lines of appropriate electrical length. For the  $\theta$ -devices directional couplers, a topology with the ability to produce high output power division ratio was used. This feature is critical for the formation of tapered output distributions producing low SLL patterns. The schematic diagram of the coupler circuit is presented in Figure 6. Two cascaded 3 dB  $90^\circ$  (branch line) couplers are connected through the  $-\theta^\circ$  and  $+\theta^\circ$  phase shifters. The value of  $\theta$  determines the output amplitude division ratio. Additional phase shifters ( $-90^\circ$  and  $+90^\circ$ ) are needed to create the proper phase progression between the output

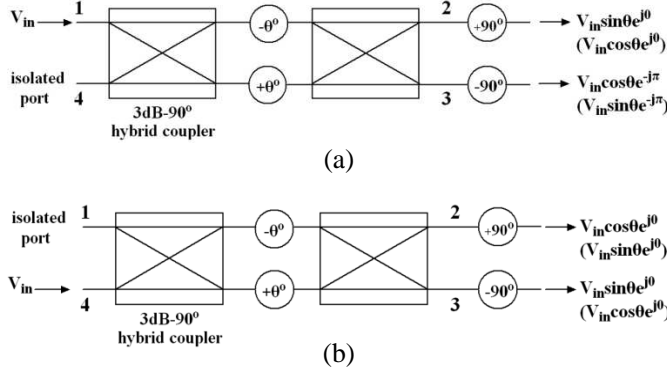


**Figure 6.** Schematic diagram of the coupler circuit used in the designs. (a) Port 1 excitation producing a  $\sin \theta / \cos \theta$  output power ratio with an  $180^\circ$  phase difference between output ports. (b) Port 4 excitation producing a  $\sin \theta / \cos \theta$  output power ratio with a uniform phase distribution.

ports, according to Figure 2. The output amplitude division ratio can be inverted, if the complementary value of  $\theta$  is used (values shown in parentheses). The analytical design procedure and simulation results are presented in the next sections.

### 3.1. $4 \times 4$ Nolen Matrix Based Network Design and Measurement

The simplest network that can be designed using the previously described procedure is a  $4 \times 4$  network. A  $-30$  dB Chebyshev distribution was chosen for a low SLL radiation pattern, whereas the phase distributions produced by the excitation of the input ports are

**Table 1.** Theoretical normalized amplitude and power coefficients of the  $-30$  dB Chebyshev distribution.

Antenna elements	Normalized amplitude distribution	Normalized power distribution	(dB)
A1	0.429	0.184	$-7.35$
A2	1	1	0
A3	1	1	0
A4	0.429	0.184	$-7.35$

similar to those produced by a corresponding  $4 \times 4$  Butler matrix (1R, 2R, 1L, 2L beams), namely four phase sequences with phase steps of  $\pm 45^\circ$  (1L and 1R beams) and  $\pm 135^\circ$  (2L and 2R beams), respectively. Network's  $\theta$  and  $\Phi$ -values are determined using the amplitude coefficients given by the  $-30$  dB Chebyshev distribution, presented in Table 1. Figure 7 shows the schematic diagram of the  $4 \times 4$  network, built by combining two separate  $2 \times 4$  subnetworks. The first  $2 \times 4$  subnetwork is designed for the 1R and 2L beams, whereas the second subnetwork is designed for the 1L and 2R beam ports. The input (beam) ports cannot be paired randomly; only the specific group of pairs is feasible, due to the limitations imposed by the conservation of energy principle. In other words, not any random combination of a pair of ports can be used to form a subnetwork. Moreover, as it was mentioned in Section 2.2, since all beams share the same array amplitude excitation ( $-30$  dB Chebyshev), the corresponding directional couplers ( $\theta$ -values) will be the same for each  $2 \times 4$  subnetwork as shown in Figure 7. On the other hand, since each input port should activate a beam with different orientation in space, which is provided by a different phase sequence excitation, the corresponding phase shifters ( $\Phi$ -values) will be different for each input port (Figure 7). Thus, when the first subnetwork is designed, the

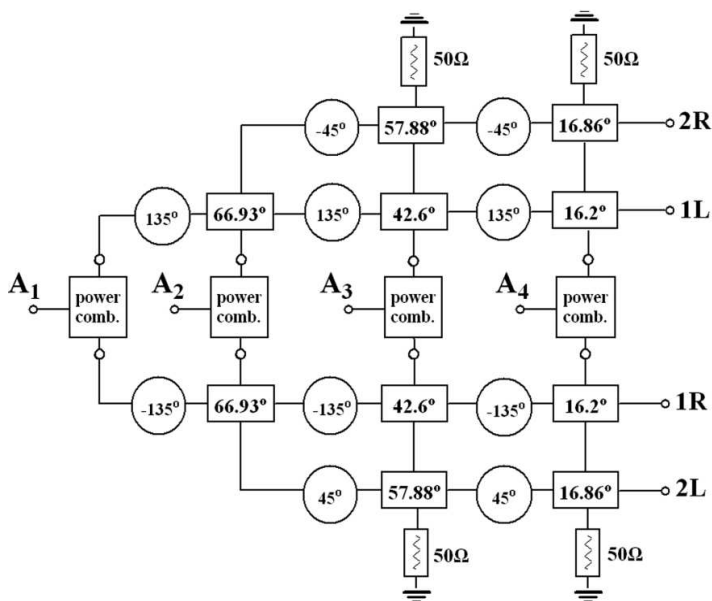


**Figure 7.** Schematic diagram of the  $4 \times 4$  network, build by combining two  $2 \times 4$  subnetworks according to Figure 5(a).

second can be designed by just inverting the corresponding  $\Phi$ -values, whereas the  $\theta$ -values remain the same. For example, the first row of the 1R-2L subnetwork demands for  $\Phi$ -values equal to  $-135^\circ$ , while the attached input port is the 1R beam port. The corresponding input port of the 1L-2R subnetwork is the 1L beam port, which creates an output phase progression with the same absolute value but with an inverse sign ( $+45^\circ$ ) to the one produced by the 1R beam port ( $-45^\circ$ ). Thus, the  $\Phi$ -values of the first row of the 1L-2R subnetwork will have the same absolute value but inverse sign ( $+135^\circ$ ) with the corresponding ones of the 1R-2L subnetwork ( $-135^\circ$ ).

As mentioned above, the basic part of the network design is the coupler circuit. Figure 8 shows the microstrip layout of one such coupler used in the network, where the  $-\theta^\circ$  and  $+\theta^\circ$  phase shifts are implemented using meandered microstrip lines with the appropriate electrical lengths. The additional  $\pm 90^\circ$  phase shifts at the outputs are incorporated into the  $\Phi$  phase shifts and the microstrip lines connecting the cascaded couplers of the network.

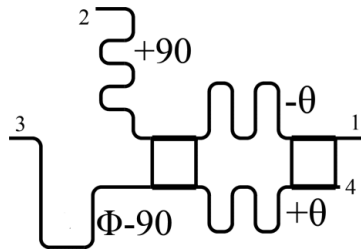


**Figure 8.** Microstrip layout of one of the coupler circuits.

A photograph of the fabricated complete network prototype is shown in Figure 9. Design frequency was set at 3 GHz, intending to develop a network for S-band applications. The circuit was developed in microstrip technology on a Rogers 4003C substrate with a dielectric constant  $\epsilon_r = 3.38$ , thickness  $h = 0.508$  mm and loss tangent  $\tan \delta = 0.0021$ . Surface mount resistor loads connected to ground through via pads were used to terminate the unused coupler ports. In order to achieve a better termination condition and a spatial symmetry, two  $100\ \Omega$  SMT chip resistors connected in parallel were used, instead of a series  $50\ \Omega$  one. Input-beam ports are named 1R, 2R, 1L, 2L (corresponding to a Butler matrix), whereas A1 to A4 ports are the output-antenna ports. In this example, Wilkinson combiners were used at the output ports (antenna inputs), trying to minimize the number of via pads (needed for the termination of the hybrid couplers' fourth port).

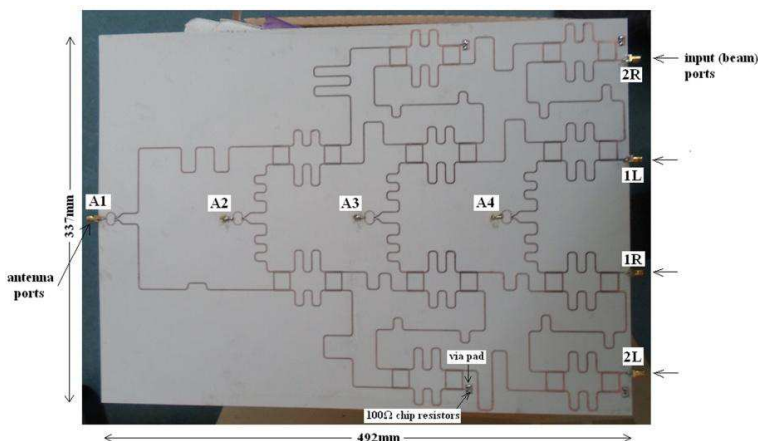


**Figure 9.** Photograph of the fabricated microstrip prototype  $4 \times 4$  Nolen matrix based network.

The design procedure for the complete network included ADS (Agilent) circuit design, optimization and simulation, along with Momentum electromagnetic simulation (MoM) of each one of the couplers and the  $\Phi$ -value microstrip lines (as the one in Figure 8). ADS circuit simulation was used for the whole network, due to the high demands of computational resources needed for MoM electromagnetic simulation of complicated and electrically large networks.

Table 2 presents the theoretical, ADS (circuit) and MoM (electromagnetic) simulated (at the center frequency of 3 GHz)  $\theta$ -values and output power division ratios of each one of the couplers of the dual-series networks of Figure 9, as the example shown in Figure 8. Table 2 shows a *very good agreement between the ADS and MoM simulated coupler power division ratios and  $\theta$ -values with their theoretically defined counterparts. Thus, ADS circuit simulation can be adopted for simulating more complicated networks.*

In order to have a better estimate of the complete network performance, we performed a Moment Method (MoM) electromagnetic simulations for the two separate dual-series ( $2 \times 4$ ) subnetwork layouts (1R-2L and 1L-2R, Figure 7), at the center frequency  $f = 3$  GHz. Electromagnetic simulation includes all physical phenomena that cannot be taken into account in circuit simulation (e.g., parasitics and mutual coupling). The results are listed in Tables 2 and 3. It can be seen that the return loss ( $S_{ii}$ ) is below  $-28$  dB, whereas the amplitude distribution is in a very good agreement with theory (Table 1).

**Table 2.** Theoretical, ADS and MoM simulated  $\theta$ -values and output power division ratio of the couplers.

Theoretical coupler $\theta$ -value ( $^\circ$ )	Theoretical output power division ratio (dB)	ADS simulated coupler $\theta$ -value ( $^\circ$ )	ADS simulated output power division ratio (dB)	MoM simulated coupler $\theta$ -value ( $^\circ$ )	MoM simulated output power division ratio (dB)
66.93	7.41	69	7.64	67.86	7.48
42.6	0.73	46.2	0.74	40.95	0.7
16.2	10.75	15.17	10.75	15.7	10.69
57.88	4.04	60.76	3.97	59.14	4.09
16.86	10.37	16.18	10.36	16.56	10.34

**Table 3.** MoM results for the separate dual-series subnetworks at center frequency  $f = 3$  GHz.

		Normalized Amplitude				(dB)			
Beam port	$S_{ii}$ (dB)	A1	A2	A3	A4	A1	A2	A3	A4
<b>1R</b>	-34.6	0.4	0.95	1	0.44	-7.96	-0.45	0	-7.1
<b>2L</b>	-28.7	0.45	0.98	1	0.45	-6.9	-0.18	0	-6.9
<b>1L</b>	-34.1	0.41	0.96	1	0.43	-7.7	-0.35	0	-7.3
<b>2R</b>	-29.3	0.42	0.97	1	0.45	-7.53	-0.26	0	-6.9

### 3.1.1. Verification of the Network through Measurements

Figure 10 shows the comparison between ADS simulated and measured results of the input return loss ( $S_{ii}$ ) magnitude, for the four input (beam) ports, as they are depicted in Figure 9. It can be observed from Figure 10 that the values of the simulated input return loss are kept well under  $-35$  dB for the center frequency of 3 GHz, whereas they remain below  $-20$  dB for about 150–200 MHz around the center frequency. Correspondingly, measured results show that the input return loss values are kept below  $-20$  dB at the center frequency for all ports, while they remain under  $-15$  dB for about 300 MHz around the center frequency ( $\approx 2.8$ – $3.1$  GHz), except for the 2R port case, which presents multiple fluctuations (but still remaining under  $-10$  dB at 2.8–3.1 GHz). Thus, the results are considered

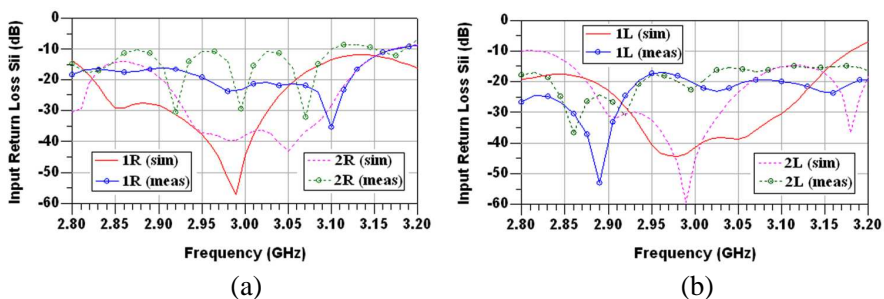


**Figure 10.** Comparison between simulated and measured input return loss ( $S_{ii}$ ) magnitude. (a) 1R and 2R input (beam) port cases. (b) 1L and 2L input (beam) port cases.

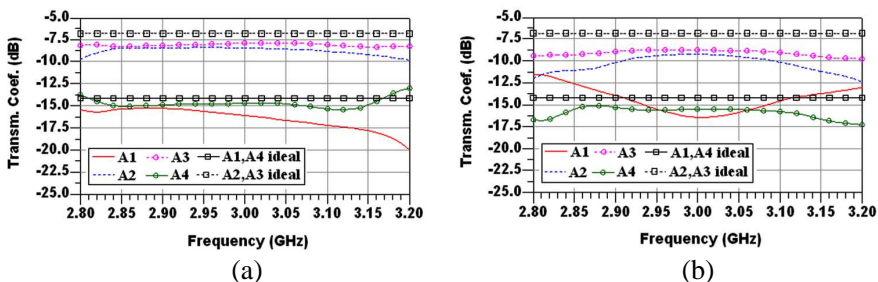


**Figure 11.** Ideal versus simulated transmission coefficients magnitudes from input ports to the antenna ports. (a) 1R beam port excitation. (b) 2R beam port excitation.

satisfying. Generally, any discrepancies observed between simulated and measured results are mainly due to the inability of the simulated model to accurately reflect all possible physical phenomena. Usually, in network (circuit) simulations some parasitic reactances are missed as well as some unpredictable mutual couplings occurring due to closely located microstrip line sections in the final layout. Moreover, possible fabrication inaccuracies regarding the dimensions of the microstrip lines could also contribute to discordances between simulation and measurement.

To produce a low SLL radiation condition, the  $-30$  dB Chebyshev distribution that was chosen, must be achieved. Figure 11 presents the simulated  $S$ -parameters results of the transmission coefficients magnitude to the four output-antenna ports, A1 to A4 (Figure 9) when 1R and 2R beam ports are excited. The ideal theoretical curves are also

depicted, for the center (A2, A3) and edge (A1, A4) antenna elements. The ideal magnitude value of the transmission coefficient is  $-6.8$  dB for the center antenna elements and  $-14.2$  dB for the edge antenna elements. It must be stated again that even the ideal values include 3 dB dissipative losses due to the use of Wilkinson power combiners in the network. These losses are not unexpected, since they are compliant with the theory of lossy low SLL multibeam networks, referred in previous sections.

Simulation results present a maximum deviation (losses) of about 2.5 dB from the ideal values, for the worst case of A1 antenna element. As it was expected, the antenna elements which are placed further from the input port (A1, A2) present greater deviation due to the fact that the losses are continuously increasing as the signal path length from the input increases. This is generally observed in all serial networks. Since the A1 and A4 antennas are placed symmetrically to the array center, they must be fed with the same power. However, the A1 antenna element will be fed with a smaller amount of power than the A4, due to its larger path length from the input port. If that effect is large enough to be able to deform significantly the predefined output amplitude distribution, it must be taken into account during the initial stages of the design. That is, the initial amplitude distribution must be redefined, dictating gradually larger percentages of power to be delivered to the antenna elements placed further, in order to account for the expected losses at their corresponding paths. Practically, that means that the network must be designed in order to feed these elements with an amount of power larger than that defined by the theoretical distribution. This additional amount of power is the one that will be dissipated along the paths leading to the antenna elements, compensating for losses that would deform the initial amplitude/power distribution and thus, balancing the effects of long signal paths. As a result, the furthest placed antenna elements will be fed with the proper amount of power dictated by the initial theoretical amplitude/power distribution.

Theoretical data for the transmission coefficients magnitudes derived by the  $-30$  dB Chebyshev distribution, dictate that the amplitude ratio between the center and edge antenna elements must be equal to 7.35 dB (Table 1). Simulations showed that this ratio is 7.2 dB for the 1R beam port, 6.9 dB for the 2R beam port, 7.3 dB for the 1L beam port and 6.7 dB for the 2L beam port, hence they are indeed satisfactory.

Two comparative examples for the transmission coefficients data are presented in Figure 12, showing simulated and measured results, for two characteristic cases of 1R and 2R port excitation. Deviations

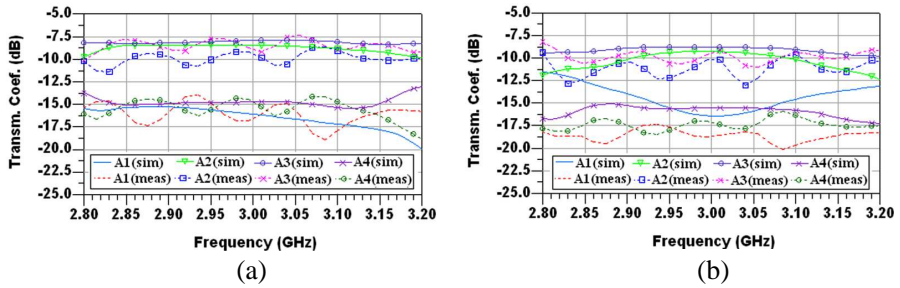


**Figure 12.** Simulated versus measured transmission coefficients magnitudes for all the A1-A4 antenna ports. (a) 1R beam port excitation. (b) 2R beam port excitation.

of measured values from the simulated ones are due to microstrip, substrate and microwave connector losses. These losses range from about 1dB to 2.5dB, for the worst cases. Although they are significant, they can be balanced by using power amplifiers in the transmitter, as most modern systems do. The power amplifiers can be used at the input port level, or more efficiently, at the antenna element level, creating an active antenna array configuration and thus, increasing system’s power efficiency. Table 4 summarizes the normalized amplitude distributions at the output-antenna ports, for all four beam port cases, as they are derived from the simulated and measured *S*-parameters data (transmission coefficients magnitudes). Table 5 presents the simulated and measured phase difference values

**Table 4.** Normalized amplitude distributions created by each input-beam port at the output-antenna ports.

		Normalized amplitude distribution (theoretical values in parentheses)			
Beam port		A1 (0.429)	A2 (1)	A3 (1)	A4 (0.429)
1R	Sim.	0.398	0.93	1	0.455
	Meas.	0.392	0.94	1	0.518
2L	Sim.	0.443	0.95	1	0.468
	Meas.	0.359	0.91	1	0.411
1L	Sim.	0.375	0.92	1	0.455
	Meas.	0.385	0.93	1	0.519
2R	Sim.	0.418	0.95	1	0.468
	Meas.	0.352	0.94	1	0.430

**Table 5.** Theoretical, simulated and measured phase difference values between antenna ports.

Beam port	Theoretical $\Delta\varphi$ ( $^\circ$ )	Simulated $\Delta\varphi$ ( $^\circ$ )			Measured $\Delta\varphi$ ( $^\circ$ )		
		A2-A1	A3-A2	A4-A3	A2-A1	A3-A2	A4-A3
1R	-45	-45.4	-45.2	-45.1	-47.6	-50.4	-44.2
2L	+135	+135	+134.9	+134.8	+130.9	+139.5	+123.8
1L	+45	+44.6	+44.8	+44.9	+48.6	+42.9	+38.4
2R	-135	-135	-135.1	-135.2	-143.2	-139.1	-133.4

between adjacent antenna ports in comparison with the theoretical ones. Despite the afore-mentioned losses that the measured data present, the amplitude ratio between center and edge elements is well maintained to acceptable levels. That means that the Chebyshev distribution is preserved, which is the most critical feature for the creation of low SLL radiated beams. The derived average measured amplitude ratio between center and edge elements is 6.7 dB for the 1R beam port, 7.94 dB for the 2R beam port, 6.7 dB for the 1L beam port and 7.65 dB for the 2L beam port.

It must be noted that, it was decided not to compensate the design, in order to balance the possible effects of the increasing losses for the antennas placed further from the input ports, as it was discussed earlier. Simulated data in Tables 3 and 4 showed that the output amplitude distribution is not critically deformed, thus, the effects on the radiation pattern are not expected to be crucial, as it will be shown in the next section. Moreover, although measured results for the A1 and A2 antenna ports present some deviations, they do not impose critical deformations in the radiation patterns.

Finally, due to the relatively increased losses of the network, it is very useful to evaluate its power efficiency. Due to the use of the Wilkinson power combiners which add a 3 dB loss, network's maximum efficiency is 50%. Under this condition, the efficiency of the network is expected to be below 50% (due to microstrip, substrate and connector losses). Thus, network's efficiency was calculated for both simulation and measurements cases, comparing simulated and measured  $S$ -parameters (transmission coefficients) magnitudes with the ideal ones. The calculated values were reduced by 50%, to include the dissipative losses that are already present in the ideal curves (Figure 11). As a result, by exploiting both simulated and measured data, the total power efficiency calculated from simulated data is about 33%, while the total power efficiency calculated from measured data is about 27.5%. Although these numbers look relatively low, the losses

can be balanced using power amplifiers, either at the network’s input port level or preferably at the antenna element level, in an active antenna configuration, as already mentioned in this section.

### 3.1.2. Radiation Patterns of the 4-element Linear Phased Array

The simulated and measured data shown in Tables 4 and 5, derived from the simulated and measured  $S$ -parameters respectively, were used as input data (excitation coefficients) in an antenna array simulation tool to produce the corresponding radiation patterns. Rectangular microstrip antenna elements were used to form the antenna array, placed initially at an inter-element distance ( $d$ ) of half free-space wavelength ( $\lambda_o/2$ ). Even though it is assumed that  $d = \lambda_o/2$  is the condition to avoid grating lobes, [2, Page 27], it is actually a situation where the grating lobe maximum is oriented towards the horizon ( $\theta_p = 90^\circ$ ). However, an arbitrary part of this lobe remains within the element pattern. How strong this contribution will be depends on the scan angle ( $\theta_o$ ) and the antenna element beamwidth. As the scan angle is increased (main lobe maximum turned away from broadside), while the antenna element pattern remains broadside as usual, this grating lobe contribution is also increased. Thus herein a more strict condition is adopted, namely to further decrease the inter-element distance so that the grating lobe contribution not to exceed the level of the highest sidelobe.

In order to prove the above concept, first  $d = \lambda_o/2$  is elaborated. Figure 13 shows comparison of the simulated radiation patterns of

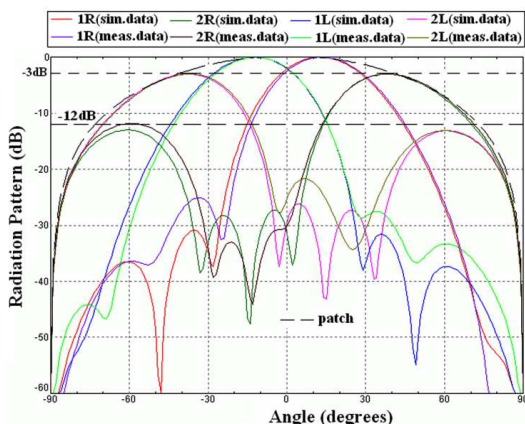


**Figure 13.** Comparison of simulated radiation patterns produced by simulated and measured  $S$ -parameters data, for an inter-element distance  $d = \lambda_o/2$ .

the four beams, produced by both simulated and measured data. Radiation patterns produced by the measured data depict some deviations from the results of simulated data, as expected. Firstly, it must be noted that the use of microstrip patch elements induces a pattern deterioration to the radiated beams, especially to the far outermost ones (2R, 2L), because the patch radiation pattern is not omnidirectional, but its maximum remains at broadside; thus, its maximum value (and directivity) is reduced with scanning angle. This condition is depicted in Figure 13, where the patch radiation pattern is depicted as the envelope of the array radiated beams. Although this fact imposes a relative degradation to the 2R and 2L beam maxima, along with their corresponding grating lobes, it relatively increases the first and second sidelobe levels, which are placed closer to broadside (where the patch radiation pattern has its maximum value). Moreover, as can be observed in Figure 13, the patch effect produces an SLL lower than expected by 1–2 dB for the simulated data patterns, leading to a value of about  $-32$  dB, for the 1R and 1L beam cases. Likewise, the 1L beam produced by the measured data presents an SLL of about  $-28$  dB, and the 1R measured data beam SLL is at about  $-25$  dB. On the other hand, the 2R and 2L beams produced by the simulated data present an SLL of about  $-24$  dB, due to the patch effect, whereas the grating lobe contribution is at  $-10$  dB with respect to the beams' maxima ( $-3$  dB level). Correspondingly, the 2R beam produced by the measured data has an SLL at about  $-27$  dB (with respect to the beam's maximum), whereas the grating lobe level is at about  $-9$  dB (with respect to the beam's maximum;  $-12$  dB in absolute value). The 2L beam produced by the measured data presents an SLL of about  $-19$  dB, while grating lobe level is preserved at  $-10$  dB (with respect to the beam's maximum). The  $-3$  dB line is shown as a lower limit for both the Crossover Level (CL) and the beam maxima value. It can be seen that the CL for the 1R and 1L beams (both from simulated and measured data) has been increased to the value of  $-2$  dB, whereas the beams are not orthogonal. In similar networks with uniform amplitude distributions (e.g., Butler and Nolen matrix) the CL is at about  $-4$  dB, whereas the beam orthogonality is maintained. As for the beam maxima of the 2R and 2L beams (both from simulated and measured data), which are degraded to  $-3$  dB, this can be surpassed by using a power control system. That is, the power transmitted in these beams can be respectively increased, balancing the effect caused by the patch antenna. Moreover, an important feature is that the beams' maxima angles are maintained, since there is an almost perfect coincidence between simulated and measured data results. Finally, most nulling angles are also preserved, with values lower than  $-35$  dB

for the simulated data and lower than  $-25$  dB for the measured data radiation patterns, for all beam cases.

However, among the above characteristics, the one that constitutes the radiation patterns presented in Figure 13 is the relatively high grating lobe level contribution for the outermost beams. The most common method for the reduction of grating lobe level is the decrease of inter-element distance ( $d$ ), aiming at reducing its contribution to the level of the highest sidelobe [1]. Less common and more complex methods include the use of angular filters [2], or placement of radiation pattern nulls at the grating lobe angle [1]. Although controlling the inter-element distance of the array is the simplest and most effective way to reduce the undesirable grating lobe level, in fact, decreasing the inter-element distance places the rising grating lobe out of the visible space. Generally, as mentioned above, the inter-element distance can be adjusted so that the grating lobe level is equal to the SLL. However, decreasing the inter-element distance also causes degradation in the array directivity. Hence, a careful compromise must be sought to decrease it only as far as required.

Thus, in this work, in order to suppress the grating lobe level contribution, the inter-element distance  $d$  was gradually decreased until the simulation results were satisfying. The final value of  $d$  was chosen equal to  $2\lambda_o/5$ . The corresponding simulated radiation patterns using both simulated and measured data are presented in Figure 14. As can be observed, the beams' maxima angles are slightly shifted, comparing

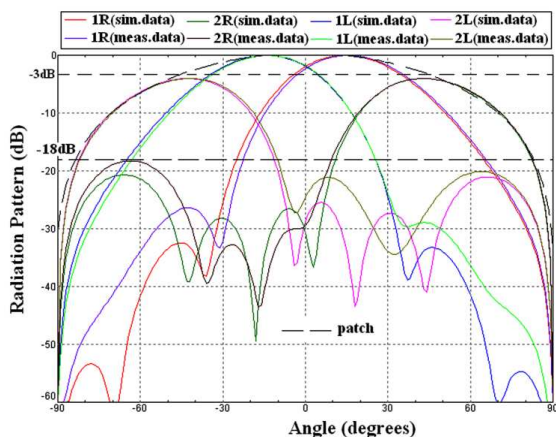


**Figure 14.** Comparison of simulated radiation patterns produced by simulated and measured  $S$ -parameters data, for an inter-element distance  $d = 2\lambda_o/5$ .

with Figure 13. Especially for the 2R and 2L beams, due to the fact that their maxima are shifted about  $7^\circ$  towards endfire, they get under further degradation, reaching a maximum value of  $-4$  dB ( $-3$  dB in Figure 13). For the simulated data, the grating lobe level is reduced to about  $-17$  dB (with respect to the  $-4$  dB of the beams' maxima). For the measured data, the corresponding grating lobe level is under  $-14$  dB (with respect to the beams' maxima), being kept under  $-18$  dB (in absolute values). Thus, there is an overall improvement (reduction) of more than 5 dB in grating lobe contribution. Moreover, the decrease in inter-element distance imposes an increase in Half-Power Beamwidth (HPBW) of the beams, which is increased from an overall average (simulated and measured data) value of  $32.1^\circ$  to the value of  $37.3^\circ$  ( $5.2^\circ$ ,  $\approx 16\%$ ). Thus, a consequent decrease in directivity is observed, which is decreased from an overall average value of 11.3 dBi to the value of 10.8 dBi (0.5 dB,  $\approx 4\%$ ).

Although further decrease in inter-element distance would produce an even lower grating lobe level, it would create beams with extremely high HPBW and low gain/directivity. Thus, the value of  $d = 2\lambda_o/5$  was chosen in order to compromise all the above conditions.

Lastly, it must be emphasized that if the effects of the patch and the losses on the SLL should be removed, a 3–5 dB even lower amplitude distribution should be chosen at the initial design level (e.g.,  $-33$  dB Chebyshev), in order to balance the expected patch effect and microstrip fabrication losses.

### 3.2. $8 \times 8$ Nolen Matrix Based Network

The same design procedure, as analyzed in the previous section, can be applied to the implementation of larger networks. This section exemplifies the design of an  $8 \times 8$  network composed of four dual-series subnetworks and synthesized gradually as explained in Section 2.2 and shown in Figures 4–5. The beams created by this network are similar to the beams created by the corresponding  $8 \times 8$  Butler matrix (1R, 2R, 3R, 4R, 1L, 2L, 3L, 4L beams), producing output phase sequences of  $\pm 22.5^\circ$  (1L and 1R beams),  $\pm 67.5^\circ$  (2L and 2R beams),  $\pm 112.5^\circ$  (3L and 3R beams) and  $\pm 157.5^\circ$  (4L and 4R beams) respectively, whereas a  $-30$  dB Chebyshev distribution was also chosen for a low SLL operation. The theoretical normalized amplitude and power coefficients of the  $-30$  dB Chebyshev distribution are presented in Table 6.

The couplers'  $\theta$ -values for the dual-series subnetworks are depicted in Table 7. They are the same for all four dual-series ( $2 \times 8$ ) subnetworks, due to the same output amplitude distribution produced, as it was mentioned in previous sections. Due to the constraints

**Table 6.** Theoretical normalized amplitude and power coefficients of the  $-30$  dB Chebyshev distribution ( $8 \times 8$  network).

Antenna elements	Normalized amplitude distribution	Normalized power distribution	(dB)
A1	0.262	0.069	$-11.6$
A2	0.519	0.269	$-5.7$
A3	0.812	0.66	$-1.8$
A4	1	1	0
A5	1	1	0
A6	0.812	0.66	$-1.8$
A7	0.519	0.269	$-5.7$
A8	0.262	0.069	$-11.6$

**Table 7.**  $\theta$ -values of the coupler circuits for the formation of the  $-30$  dB Chebyshev amplitude distribution.

$\theta$ -values						
$\theta_{1,1}$	$\theta_{1,2}$	$\theta_{1,3}$	$\theta_{1,4}$	$\theta_{1,5}$	$\theta_{1,6}$	$\theta_{1,7}$
$63.19^\circ$	$54.4^\circ$	$45.05^\circ$	$35.29^\circ$	$25.13^\circ$	$15.18^\circ$	$7.54^\circ$
	$\theta_{2,1}$	$\theta_{2,2}$	$\theta_{2,3}$	$\theta_{2,4}$	$\theta_{2,5}$	$\theta_{2,6}$
	$58^\circ$	$49.4^\circ$	$37.5^\circ$	$26.4^\circ$	$15.54^\circ$	$7.62^\circ$

**Table 8.**  $\Phi$ -values needed for all four dual-series subnetworks (1R-4L, 1L-4R, 2R-3L, 2L-3R).

Dual series ( $2 \times 8$ ) subnetworks	$\Phi$ -values	
	$\Phi_{1,n}$ row	$\Phi_{2,n}$ row
<b>1R-4L</b>	$-157.5^\circ$	$+22.5^\circ$
<b>1L-4R</b>	$+157.5^\circ$	$-22.5^\circ$
<b>2R-3L</b>	$-112.5^\circ$	$+67.5^\circ$
<b>2L-3R</b>	$+112.5^\circ$	$-67.5^\circ$

mentioned in previous sections, the only valid dual-series ( $2 \times 8$ ) subnetworks that can be designed are the 1R-4L, 1L-4R, 2R-3L, and 2L-3R. Accordingly, the phase shifters'  $\Phi$ -values for each of the above  $2 \times 8$  subnetworks are tabulated in Table 8. Hence, the corresponding dual-series ( $2 \times 8$ ) subnetworks are obtained. The  $2 \times 8$  subnetworks are connected in pairs into  $4 \times 8$  subnetworks. Figure 15(a) shows the schematic diagram of the 1R-4L-2R-3L  $4 \times 8$  subnetwork. Obviously, the other  $4 \times 8$  subnetwork is created using the rest two  $2 \times 8$

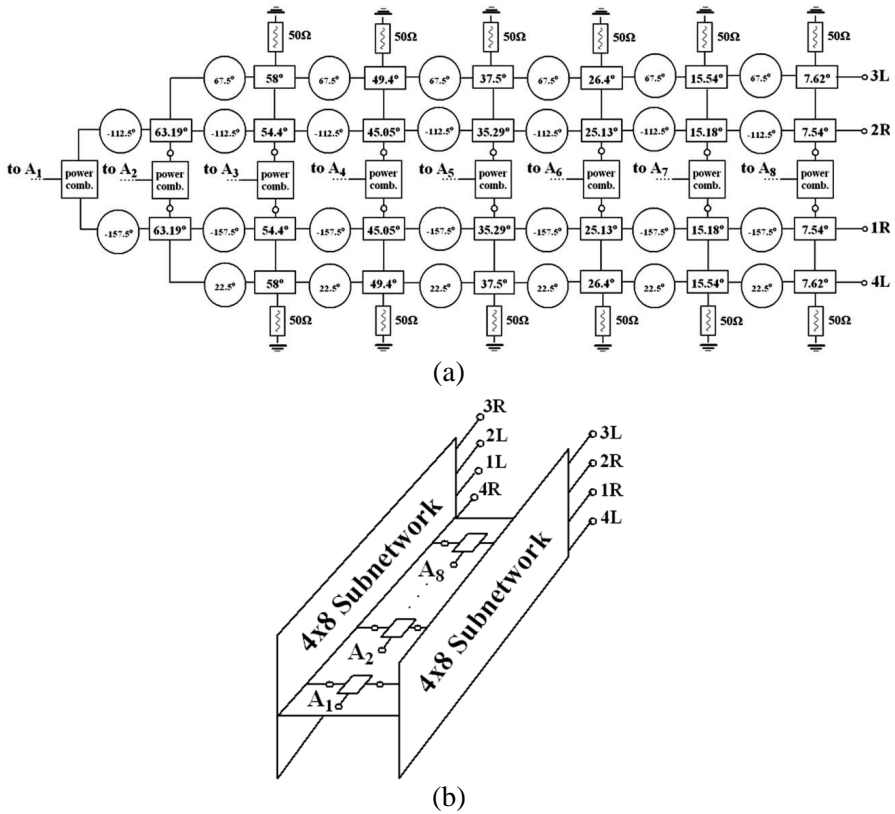


**Figure 15.** (a) Schematic diagram of the 1R-4L-2R-3L  $4 \times 8$  subnetwork, composed of the 1R-4L and 2R-3L dual-series ( $2 \times 8$ ) subnetworks. (b) Schematic diagram of the whole  $8 \times 8$  matrix configuration, composed of the two  $4 \times 8$  subnetworks.

subnetworks, meaning that it is the 1L-4R-2L-3R subnetwork. In turn, the two  $4 \times 8$  subnetworks are connected using the Wilkinson power combiners to create the whole  $8 \times 8$  matrix configuration, as presented in Figure 15(b), in accordance with the general case shown in Figure 5(b).

Figure 16 shows the simulated (using ADS) transmission coefficients from the input ports to the antenna elements, of the ideal  $8 \times 8$  network, without microstrip losses. Table 9 lists the normalized output amplitude/power distribution values, derived from the simulated results of Figure 16.

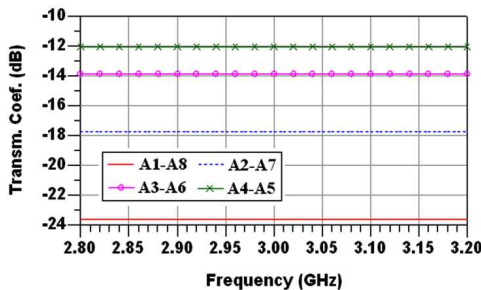


**Figure 16.** Simulated transmission coefficients from the input ports to the antenna elements, of the ideal (ignoring microstrip losses)  $8 \times 8$  network.

**Table 9.** Simulated normalized amplitude and power coefficients of the  $-30$  dB Chebyshev distribution ( $8 \times 8$  network).

Antenna element	Normalized amplitude	Normalized power	(dB)
A1	0.263	0.069	-11.6
A2	0.516	0.266	-5.75
A3	0.808	0.653	-1.85
A4	1	1	0
A5	1	1	0
A6	0.808	0.653	-1.85
A7	0.516	0.266	-5.75
A8	0.263	0.069	-11.6

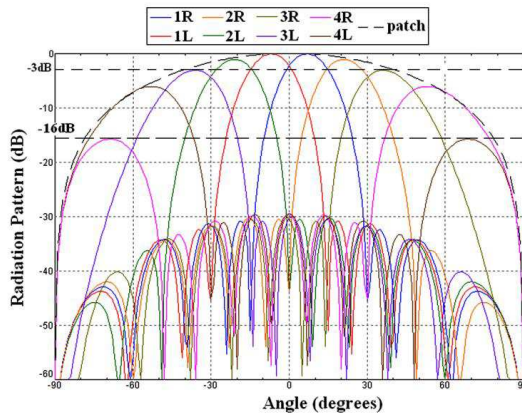
### 3.2.1. Radiation Patterns of the 8-element Linear Phased Array

Figure 17 shows the radiation patterns produced by the simulation of an ideal  $8 \times 8$  network feeding an eight-element patch antenna array with an inter-element distance  $d = \lambda_o/2$ . The patch antenna effect is again observed, placing the 3R, 4R, 3L and 4L beams maxima below the limit level of  $-3$  dB (once again the transceiver power control mechanism must be utilized in order to exploit these beams). SLL is well kept under  $-30$  dB, apart from the grating lobes that appear in the 4R and 4L beams. The grating lobe level is at  $-10$  dB, with respect to the outermost beam’s maximum ( $-6$  dB). The Crossover Level of the beams closer to broadside (1R and 1L), suffering no degradation, is at  $-2$  dB.

In order to reduce the relatively high grating lobe level of the outermost beams in Figure 17, the inter-element distance ( $d$ ) is again adjusted in order to achieve a grating lobe level equal to the sidelobe level. Successive decreases in  $d$  and corresponding simulations led to a

value of  $d = 17\lambda_o/40$ . The simulation results are shown in Figure 18. Comparing with the results of Figure 17, it is observed that the average HPBW of the 8 beams is increased from  $18.9^\circ$  to  $21.9^\circ$  ( $3^\circ$ ,  $\approx 16\%$ ), corresponding to an average directivity degradation from 13.9 dBi to 13.6 dBi (0.3 dB, 2%).

In this case, due to the larger electrical length of the array, the increase in HPBW (and decrease in gain/directivity) is not substantial, in comparison with the 4-element array of the previous section. Again, a slight angular shift in the beams' maxima is observed, leading the 3R and 3L beams below the  $-3$  dB limit. However, the grating lobe level of the 4R and 4L beams is reduced to  $-20$  dB with respect to the corresponding beams' maxima ( $-7$  dB).



**Figure 17.** Simulated radiation patterns produced by an ideal  $8 \times 8$  network, for an inter-element distance  $d = \lambda_o/2$ .

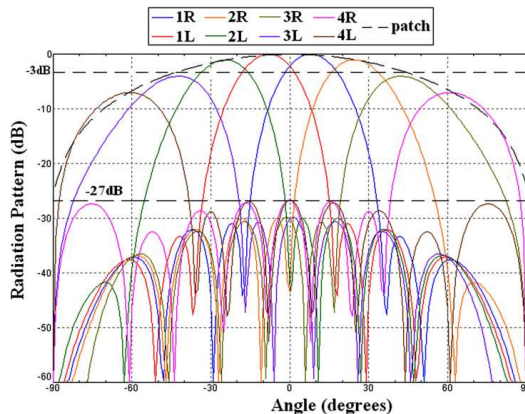


**Figure 18.** Simulated radiation patterns produced by an ideal  $8 \times 8$  network, for an inter-element distance  $d = 17\lambda_o/40$ .

### 3.3. $4 \times 8$ Nolen Matrix Based Network Design for Direction-of-arrival Measurements

The previously described design procedure can also be applied to networks with an unequal number of input ( $M$ ) and output ( $N$ ) ports. A design example of a  $4 \times 8$  network will be given herein. Since the network is a four input-beam port design, the beams that can be produced are those of a  $4 \times 4$  network (1R, 2R, 1L, 2L). The network is composed of two  $2 \times 8$  subnetworks, whereas a  $-30$  dB Chebyshev distribution is again chosen for a low SLL pattern. The  $\theta$ -values of the  $2 \times 8$  subnetworks are those given in Table 7 for the  $8 \times 8$  network, whereas the  $\Phi$ -values are the same with the  $4 \times 4$  network case (Figure 7).

The complete ideal (without microstrip losses)  $4 \times 8$  network was simulated using ADS, and as before, the  $S$ -parameters data (amplitude and phase of transmission coefficients) were used to produce the antenna array radiation patterns. Figure 19 shows the simulated radiation patterns of the four beams, for an inter-element distance  $d = \lambda_o/2$ .

As can be seen from Figure 19, the 1R and 1L beams are placed at the same angular positions with the corresponding beams of a  $4 \times 4$  network (Figure 13), whereas the 2R and 2L beams are displaced by about  $6^\circ$  towards endfire, in comparison with Figure 13. Moreover, the 2R and 2L beams maxima are now well below the  $-3$  dB limit level, having a maximum value of  $-4$  dB. However, the most critical feature of the beam cluster of Figure 19 is the extremely low Crossover Level of the beams, which for the 1R and 1L beams almost reaches the level

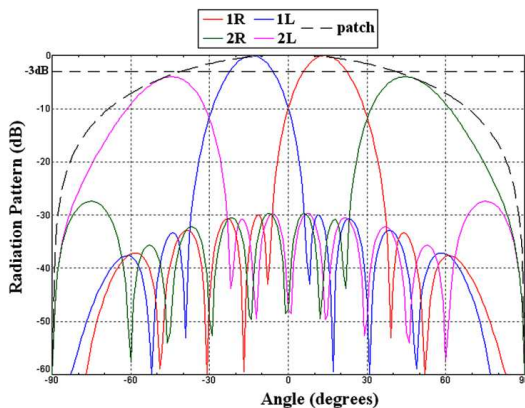


**Figure 19.** Simulated radiation patterns produced by an ideal  $4 \times 8$  network, for an inter-element distance  $d = \lambda_o/2$ .

of  $-10$  dB. This is due to the fact that the beams are placed far apart from each other, with angular distances exceeding their half-power beamwidth. However, the grating lobe level for the outermost beams ( $2R$  and  $2L$ ) is below  $-23$  dB (with respect to the beams' maxima), thus significantly improved over previous designs with the same inter-element distance ( $d = \lambda_o/2$ ), e.g., the  $8 \times 8$  network (Figure 17). Nevertheless, the sparse beam cluster of Figure 19 is unacceptable for almost any communication application, since it provides a very low scanning coverage quality of the interested angular sector. That is, the available gain around the CL points is much lower than the maximum and the radiation pattern intensity is quite low ( $\ll -3$  dB) for the largest part of the angular directions between beams' maxima. These low gain angular windows constitute a large amount of the scanning sector, creating a sparse scanning with many almost-blind angles. Even though this design is not well suited for a complete angular coverage, it could be best utilized in source tracking, e.g., for Direction-Of-Arrival (DOA) measurements.

### 3.4. $4 \times 8$ Nolen Matrix Based Network Using the Switched-line-phase-shifter Technique

A solution to the sparse beam coverage problem could be the exploitation of Switched-Line-Phase-Shifter (SLPS) technique, as used and described in our previous work [17, 24]. Figure 20 shows the schematic diagram of the  $4 \times 8$  network implementing the SLPS

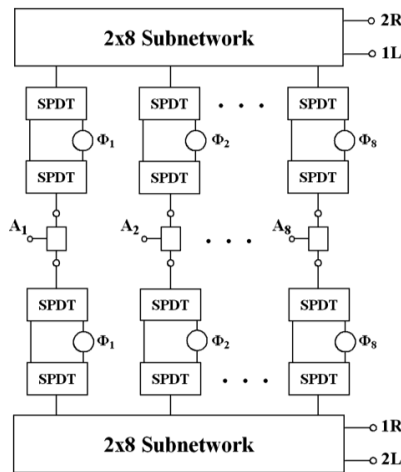


**Figure 20.** Schematic diagram of the  $4 \times 8$  network implementing the SLPS technique.

technique. The main idea is to connect additional phase shifts ( $\Phi_1$ - $\Phi_8$ ) through Single-Pole Dual-Through (SPDT) switches at the output ports, in order to be able to create additional phase progressions between the output ports. Each SLPS is composed of two SPDTs and two separate signal paths of different electrical length. The first path introduces no additional phase shift to the signal, so when it is chosen, the conventional beams of Figure 19 can be created. However, when the  $\Phi$ -paths (Figure 20) are chosen at the SLPSs, each input-beam port excitation produces a new beam which is displaced in space and points to a new angular direction. In this design, the values of the additional phase shifts are selected so that each new beam is displaced to the right of the corresponding conventional beam, excited by the respective input-beam port and points at the middle of its two neighboring beams angular distance. Figure 21 shows the simulated radiation patterns of an ideal  $4 \times 8$  network implementing the SLPS technique. As an example, the (1R, 2R) beam is created when the 1R input (beam) port is excited and the additional phase shifts are selected at the outputs. Its maximum points at the middle of the angular distance between the 1R and 2R beams. It can be seen, that 3 new beams are created, increasing the total number to 7. The CL is highly increased to  $-2$  dB for the central 1R, 1L and (1L, 1R) (broadside) beams, while the beam cluster is now densified and the scanning coverage quality of the angular sector is improved significantly. The two far outermost beams are still kept below the  $-3$  dB limit, but this can again be solved with a power control system.

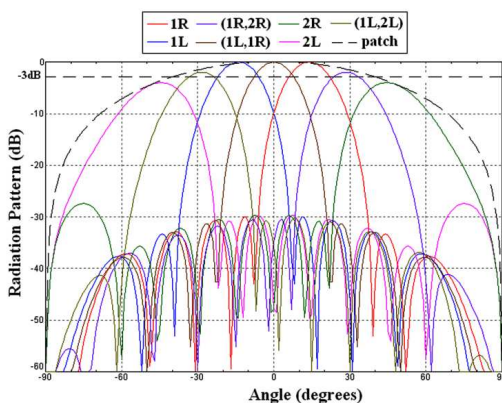


**Figure 21.** Simulated radiation patterns of an ideal  $4 \times 8$  network implementing the SLPS technique, for an inter-element distance  $d = \lambda_o/2$ .

### 3.5. Comparison between the $8 \times 8$ and $4 \times 8$ Designs

It would be very interesting to make a comparison of the  $4 \times 8$  network of Figure 20 with an  $8 \times 8$  network, as it was presented in the previous section. Firstly, although the  $8 \times 8$  network is able to create 8 radiated beams (Figures 17 and 18) instead of 7, the  $4 \times 8$  network using SLPS circuitry is able to produce a broadside beam ((1L, 1R)) (Figure 21), which it does not exist in the conventional  $8 \times 8$  beam cluster. The total angular sector of the  $4 \times 8$  network, measuring from the left  $-3$  dB point of the far left beam to the right  $-3$  dB point of the far right beam, is about  $110^\circ$ , while for the  $8 \times 8$  network is about  $130^\circ$ . The Crossover Level is almost similar for both beam clusters ( $-2$  dB), whereas the grating lobe level is significantly lower in the  $4 \times 8$  network case (especially when keeping inter-element distance equal to  $\lambda_o/2$ ). More explicitly, the grating lobe level of the  $8 \times 8$  network is at about  $-10$  dB (Figure 17), whereas for the  $4 \times 8$  network is at  $-23.5$  dB, always with respect to the corresponding beam's maximum, which is at  $-6$  dB and  $-4$  dB respectively. Thus, the  $4 \times 8$  network could be preferable over an  $8 \times 8$  one in applications where a narrower scanning sector is required and/or where the grating lobe level is of significant importance.

## 4. CONCLUSION

The analytical procedure of synthesis, design and measurement of a new type of Nolen matrix based series feed beamformers was presented. The networks are designed using a dual-series subnetwork as the basic building block. The emphasis was given on the design of tapered amplitude distribution networks for low SLL multibeam antennas. Theoretically, any random amplitude distribution can be implemented using the proposed architecture. The series feed method offers some advantages over the corporate, such as the avoidance of microstrip crossovers. Measurement results for the fabricated  $4 \times 4$  prototype are quite satisfying. Simulation results for larger networks, such as the  $8 \times 8$  and  $4 \times 8$ , were given. Future work includes the design, fabrication and measurement of larger networks with 4–8 inputs and 8–16 outputs for X- to Ka-band system applications.

## ACKNOWLEDGMENT

This research has been co-financed by the European Union (European Social Fund — ESF) and Greek national funds through the Operational Program “Education and Lifelong Learning” of the

National Strategic Reference Framework (NSRF) — Research Funding Program: **THALES**. Investing in knowledge society through the European Social Fund.

## REFERENCES

1. Hansen, R. C., *Phased Array Antennas*, 2nd Edition, John Wiley & Sons, Hoboken, New Jersey, 2009.
2. Mailloux, R. J., *Phased Array Antenna Handbook*, 2nd Edition, Artech House, Norwood, MA, 2005.
3. Ajioka, J. S. and J. L. McFarland, “Beam-forming feeds,” *Antenna Handbook; Theory, Applications and Design*, Chapter 19, Y. T. Lo and S. W. Lee, Eds., Van Nostrand Reinhold, New York, 1988.
4. Butler, J. L. and R. Lowe, “Beam forming matrix simplifies design of electronically scanned antennas,” *Electronic Design*, Vol. 9, 170–173, Apr. 1961.
5. Shelton, J. P. and K. S. Kelleher, “Multiple beams from linear arrays,” *IRE Trans. Antennas Propagat.*, Vol. 9, No. 2, 154–161, Mar. 1961.
6. Moody, H. J., “The systematic design of the Butler matrix,” *IEEE Trans. Antennas Propagat.*, Vol. 12, No. 6, 786–788, Nov. 1964.
7. Blass, J., “Multidirectional antenna — A new approach to stacked beams,” *IRE Int. Conf. Record*, Vol. 8, 48–50, 1960.
8. Nolen, J., “Synthesis of multiple beam networks for arbitrary illuminations,” Ph.D. Dissertation, Radio Division, Bendix Corp., Baltimore, MD, Apr. 1965.
9. Shelton, J. P., “Reduced sidelobes for Butler-matrix-fed linear arrays,” *IEEE Trans. Antennas Propagat.*, Vol. 17, No. 5, 645–647, Sep. 1969.
10. Li, W.-R., C.-Y. Chu, K.-H. Lin, and S.-F. Chang, “Switched-beam antenna based on modified Butler matrix with low sidelobe level,” *Electronics Letters*, Vol. 40, No. 5, 290–292, Mar. 2004.
11. Gruszczynski, S., K. Wincza, and K. Sachse, “Reduced sidelobe four-beam  $N$ -element antenna arrays fed by  $4 \times N$  Butler matrices,” *IEEE Ant. Propag. Letters*, Vol. 5, 430–434, Dec. 2006.
12. Mosca, S., F. Bilotti, A. Toscano, and L. Vegni, “A novel design method for Blass matrix beam-forming networks,” *IEEE Trans. Antennas Propagat.*, Vol. 50, No. 2, 225–232, Feb. 2002.
13. Casini, F., R. V. Gatti, L. Marcaccioli, and R. Sorrentino, “A novel design method for Blass matrix beam-forming networks,”

- Proc. 37th Europ. Microw. Conf.*, 1511–1514, Munich, Germany, Oct. 2007.
14. Fonseca, N. J. G., “Printed S-band  $4 \times 4$  Nolen matrix for multiple beam antenna applications,” *IEEE Trans. Antennas Propagat.*, Vol. 57, No. 6, 1673–1678, Jun. 2009.
  15. Fonseca, N. J. G. and N. Ferrando, “Nolen matrix with tapered amplitude law for linear arrays with reduced sidelobe level,” *Proc. 4th Europ. Conf. Antennas Propagat.*, 1–5, Barcelona, Spain, Apr. 2010.
  16. Fakoukakis, F. E., S. G. Diamantis, A. P. Orfanides, and G. A. Kyriacou, “Development of an adaptive and a switched beam smart antenna system for wireless communications,” *Journal of Electromagnetic Waves and Applications*, Vol. 20, No. 3, 399–408, 2006.
  17. Fakoukakis, F. E. and G. A. Kyriacou, “On the design of a Butler matrix-based beamformer introducing low sidelobe level and enhanced beam-pointing accuracy,” *Proc. IEEE-APS Top. Conf. Antennas Propagat. Wirel. Comm.*, 1265–1268, Torino, Italy, Sep. 2011.
  18. Fakoukakis, F. E., G. A. Kyriacou, and J. N. Sahalos, “On the design of Butler-like type matrices for low SLL multibeam antennas,” *Proc. 6th Europ. Conf. Antennas Propagat.*, 2604–2608, Prague, Czech Republic, Mar. 2012.
  19. Jones, W. R. and E. C. Dufort, “On the design of optimum dual-series feed networks,” *IEEE Trans. Microw. Theory & Techn.*, Vol. 19, No. 5, 451–458, May 1971.
  20. Allen, J. L., “A theoretical limitation on the formation of lossless multiple beams in linear arrays,” *IRE Trans. Antennas Propagat.*, Vol. 9, No. 4, 350–352, Jul. 1961.
  21. White, W. D., “Pattern limitations in multiple-beam antennas,” *IRE Trans. Antennas Propagat.*, Vol. 10, No. 4, 430–436, Jul. 1962.
  22. DuFort, E. C., “Optimum low sidelobe high crossover multiple beam antennas,” *IEEE Trans. Antennas Propagat.*, Vol. 33, No. 9, 946–954, Sep. 1985.
  23. Stein, S., “On cross-coupling in multiple beam antennas,” *IEEE Trans. Antennas Propagat.*, Vol. 10, No. 5, 548–557, Sep. 1962.
  24. Gotsis, K. A., G. A. Kyriacou, and J. N. Sahalos, “Improved Butler matrix configuration for smart beamforming operations,” *Proc. 4th Europ. Conf. Antennas Propagat.*, 1–4, Barcelona, Spain, Apr. 2010.